Experimental verification of dispersed fringe sensing as a segment phasing technique using the Keck telescope

Fang Shi, Gary Chanan, Catherine Ohara, Mitchell Troy, and David C. Redding

Dispersed fringe sensing (DFS) is an efficient and robust method for coarse phasing of segmented primary mirrors (from one quarter of a wavelength to as much as the depth of focus of a single segment, typically several tens of microns). Unlike phasing techniques currently used for ground-based segmented telescopes, DFS does not require the use of edge sensors in order to sense changes in the relative heights of adjacent segments; this makes it particularly well suited for phasing of space-borne segmented telescopes, such as the James Webb Space Telescope. We validate DFS by using it to measure the piston errors of the segments of one of the Keck telescopes. The results agree with those of the Shack–Hartmann-based phasing scheme currently in use at Keck to within 2% over a range of initial piston errors of ± 16 μm. © 2004 Optical Society of America

OCIS codes: 010.7350, 120.5050, 220.1140.

1. Introduction

The importance of phasing segmented mirror telescopes is generally appreciated: The resolution of a poorly phased telescope can be no greater than the diffraction limit corresponding to a segment, as opposed to the diffraction limit of the full aperture in the well-phased case.

For the Keck telescopes, the prototypes of ground-based segmented telescopes, the segment phasing problem is solved in two different ways: (1) a modified Shack–Hartmann technique[1,2] and (2) a modified curvature sensing technique.[3] Both of these approaches rely on the well-calibrated (in a relative, not absolute, sense) segment edge sensors at Keck. However, these techniques are not directly applicable to space-based segmented telescopes, such as the James Webb Space Telescope (JWST), because there are no edge sensors in the baseline JWST design. Dispersed fringe sensing, or DFS, is intended to solve the segment phasing problem subject to this restriction.

DFS is an effective method for phasing any segmented mirror system and has been validated extensively on several small-scale laboratory test beds. On the JWST Wavefront Control Testbed we demonstrated closed-loop DFS performance with an accuracy of 50 nm and a capture range of 100 μm.[4,5] The DFS algorithm also performs well in computer simulations of the JWST 18-hexagon design, the Developmental Comparative Active Telescope Testbed (DCATT), and the double-pass JWST optical testing system at the Plum Brook Station in Sandusky, Ohio. In this paper we use the Keck telescope as a test bed and compare DFS directly with the Shack–Hartmann-based phasing scheme that has successfully been used for the past decade at Keck.

This paper is organized as follows. In Section 2 we present the theory of DFS in the context of applications to segmented mirrors. In Section 3 we describe the Keck telescopes, the Keck phasing camera system[6] (PCS), and the modifications to the PCS hardware used for the current tests. In Sections 4 and 5 we describe the experimental procedure and data analysis, respectively. In Sections 6 and 7 we describe our results and present our conclusions, respectively.

2. Theory of Dispersed Fringe Sensing

In this section we give an approximate but general derivation of the basic equation of DFS. We begin

F. Shi (shi@s383.jpl.nasa.gov), C. Ohara, M. Troy, and D. C. Redding are with the Jet Propulsion Laboratory, California Institute of Technology, 4800 Oak Grove Drive, Pasadena, California 91109. G. Chanan is with the Department of Physics and Astronomy, University of California, Irvine, California 92697.

by considering monochromatic radiation of wavelength $\lambda = 2\pi/k$. Let $\boldsymbol{\omega}$, with rectangular coordinates (x, y) in radians, be the position vector in the image plane. We consider a circular subaperture of diameter d, split down the middle by the line $\eta = 0$ in the aperture plane, where η is the coordinate corresponding to y in the image plane. The upper semicircular segment ($\eta > 0$) has a piston error of $\delta/2$, and the lower semicircular segment ($\eta < 0$) has a piston error of $-\delta/2$. Thus δ is the physical step height; the corresponding optical path difference is 2δ. We have shown elsewhere[1] that the intensity in the image plane is

$$I(\boldsymbol{\omega}; k\delta) = [\hat{f}(\boldsymbol{\omega}; 0)\cos(k\delta) + \hat{f}(\boldsymbol{\omega}; \pi/2)\sin(k\delta)]^2, \quad (1)$$

where $\hat{f}(\boldsymbol{\omega}; 0)$ is the complex amplitude that results when the two segments are in phase (i.e., corresponds to the familiar Airy disk) and $\hat{f}(\boldsymbol{\omega}; \pi/2)$ is the complex amplitude when the two segments are one-half wave out of phase ($\delta = \lambda/4$). The precise form of $\hat{f}(\boldsymbol{\omega}; \pi/2)$ (as well as other relevant details of the discussion) may be found in Ref. 1. For our purposes here it is necessary only to note that $\hat{f}(\boldsymbol{\omega}; \pi/2)$, like $\hat{f}(\boldsymbol{\omega}; 0)$, is a well-behaved function whose angular extent in the x direction is approximately λ/d. It is convenient to rewrite Eq. (1) as

$$I(\boldsymbol{\omega}; k\delta) = I_1(\boldsymbol{\omega}) + I_2(\boldsymbol{\omega})\sin(2k\delta) + I_3(\boldsymbol{\omega})\cos(2k\delta), \quad (2)$$

where $I_i(i = 1, 2, 3)$ all have width $\sim\lambda/d$ in the x direction. In general we define the visibility γ of I as

$$\gamma = (I_{max} - I_{min})/(I_{max} + I_{min}). \quad (3)$$

For the undispersed fringe of Eq. (1) or (2), with I considered as a function of k, we have $\gamma = 1$. Equivalently, the I_i are related by

$$I_1^2 = I_2^2 + I_3^2. \quad (4)$$

To measure the phase error between adjacent mirror segments, DFS uses a grism—a transmission grating replicated onto a prism—to disperse the light from a broadband source into a spectrum of wavelengths on the detector. The grism disperses the fringe linearly along the dispersion direction x:

$$\lambda(x) = \lambda_0 + \frac{\partial\lambda}{\partial x}x = \lambda_0 + C_0 x, \quad (5)$$

where λ_0 is the central wavelength and C_0 is the dispersion coefficient of the grism in meters per radian. Now we consider a distribution of wavelengths and make use of Eq. (5). We assume that the wavelength spectrum is reasonably flat on a scale

over which $k\delta$ varies by π. At a nominal location $\boldsymbol{\omega}$ on the detector, the intensity will be given by

$$I(\boldsymbol{\omega}) = \int [I_1(\boldsymbol{\omega} - \boldsymbol{\omega}') + I_2(\boldsymbol{\omega} - \boldsymbol{\omega}')\sin(2k\delta)$$
$$+ I_3(\boldsymbol{\omega} - \boldsymbol{\omega}')\cos(2k\delta)]dx', \quad (6)$$

where $\boldsymbol{\omega}' = (x', 0)$ lies along the x' (dispersion) direction and k is related to x by Eq. (5), or approximately

$$k' - k = C_0 k_0^2 (x' - x)/2\pi, \quad (7)$$

which holds for a modest range in k about the nominal value of $k_0 = 2\pi/\lambda_0$. In general we expect

$$\lambda/d \ll \delta/\lambda. \quad (8)$$

Therefore it follows that $k\delta$ varies much more rapidly with x than do the I_i. Because of this fact, and because we are more interested in the generality of our results than in the precise values of factors of order unity, we approximate the I_i as

$$I_i(\boldsymbol{\omega}) = g(x)h_i(y), \quad (9)$$

where

$$g(x) = \exp(-x^2/2\sigma^2), \quad (10)$$
$$h_1^2 = h_2^2 + h_3^2. \quad (11)$$

If we make the identification $\sigma \sim \lambda/2d$, then this approximation preserves the essential features of the problem, i.e., approximates the correct width (in x) of the diffraction patterns and the visibility condition [Eq. (4)] while at the same time admitting an analytical solution. In particular, from Eqs. (6)–(7) and (9)–(11) we have

$$I(\boldsymbol{\omega}) = I_0(y)\{1 + \exp(-\alpha^2)\cos[(2k\delta) + \phi(y)]\}, \quad (12)$$

where

$$\alpha \approx 2\sqrt{2}\pi C_0\sigma\delta/\lambda_0^2. \quad (13)$$

Because we did not assume an explicit form for the functions $\hat{f}(\boldsymbol{\omega}; 0)$ and $\hat{f}(\boldsymbol{\omega}; \pi/2)$, these results hold for a variety of aperture shapes, except that the expression for the visibility $\gamma = \exp(-\alpha^2)$ in Eq. (12) is (in all cases) only approximate. In general, therefore, we have the following fundamental equation for DFS:

$$I(\boldsymbol{\omega}) = I_0\{1 + \gamma\cos[2k\delta + \phi(y)]\}, \quad (14)$$

where I_0 is the amplitude, γ is the fringe visibility, and $\phi(y)$ is a phase term that depends on where the fringe signal is extracted. Given that the original functions $\hat{f}(\boldsymbol{\omega}; 0)$ and $\hat{f}(\boldsymbol{\omega}; \pi/2)$ are even and odd, respectively, with respect to y, it follows that $\phi(0) = 0$. The piston error δ may be determined from Eq. (14) by fitting the observed fringe intensity to δ and to the above three parameters.

Qualitatively, periodic bright or dark bands occur in the fringe pattern along the dispersed spectrum at wavelengths that satisfy (respectively) the construc-
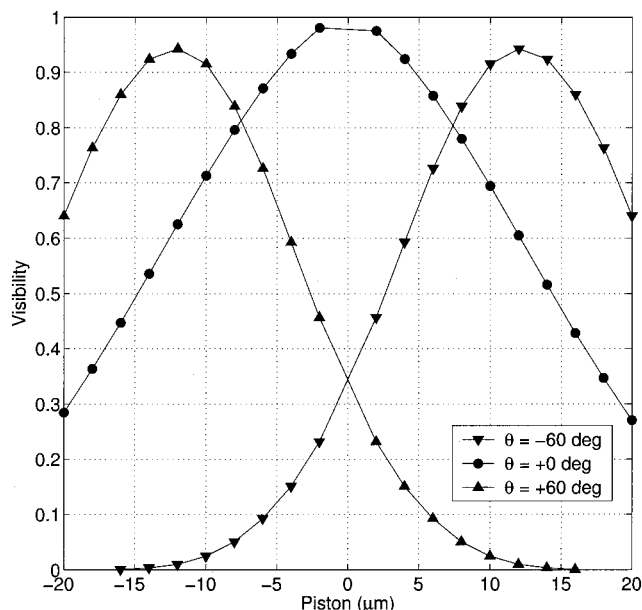
Fig. 1. Theoretical fringe visibility curves for the three different edge orientations.

Fig. 2. Simulated fringe formation for the three different edge orientations for an edge height of $+4$ μm. The display is logarithmically stretched to accentuate the diffraction effects. From bottom to top, the three pairs of fringes correspond to edge orientations of $-60°$, $0°$, and $+60°$, respectively. In each pair, the lower fringe is the result of discrete sampling and illustrates the buildup of the fringe, whereas the upper one shows the fully dispersed fringe that results from dense wavelength sampling. Note that for edges oriented at $+60°$ and for positive edge heights, the individual diffraction patterns are oriented so that they tend to fill in the dark bands on each fringe and thus to reduce the visibility. A similar effect occurs for edges oriented at $-60°$ and negative edge heights.

tive interference condition $[4\pi\delta/\lambda(x) + \phi(y)] = 2n\pi$ or the destructive condition $[4\pi\delta/\lambda(x) + \phi(y)] = (2n + 1)\pi$, where n is an integer. The number of fringes in the spectrum across a given bandwidth is proportional to the optical path difference between the mirror segments. The spatial frequency of the fringe pattern is therefore a direct measure of the magnitude of the piston error: For large errors, the fringe period is short; for perfectly phased segments, the wave front adds constructively at all wavelengths, and no fringes are observed.

From Eq. (12) and relation (13), the capture range of the DFS algorithm is bounded approximately by $\pm\delta_0$:

$$\delta_0 \approx 0.23\lambda_0 d/C_0. \qquad (15)$$

For $-\delta_0 \lesssim \delta \lesssim \delta_0$ the fringe visibility is large, but it decreases rapidly outside this range. For the nominal values of the current experiment, we have (see Section 3) $\lambda_0 = 0.75$ μm, $d = 12$ cm, $C_0 = 0.122$ cm/rad, and thus $\delta_0 \approx 17$ μm. An exact treatment of the problem, using a numerical integration of the exact function $\hat{f}$, leads to very similar results (see Fig. 1).

Because adding π to ϕ in Eq. (14) is equivalent to changing the sign of δ, it is clear that the sign of the path difference cannot be extracted from a single row of pixels (which we always assume to be aligned with the dispersion direction). The sign of δ can be extracted, however, by an examination of the signal in neighboring rows, because these rows have different values of the phase factor $\phi(y)$; we typically consider the central row and the rows immediately above and below it (three rows in all). To see this sign-dependence qualitatively and graphically, consider a single dispers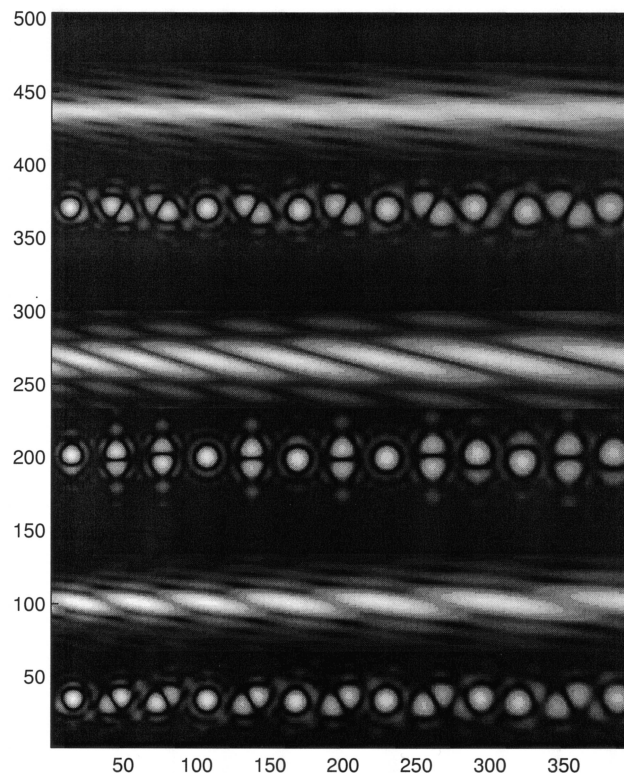ed fringe in Fig. 2. If we now imagine the entire system reflected about the x axis, it is clear that both the edge step and the slant angle of the fringe pattern (measured with respect to the x axis) will change sign.

Detailed considerations show that DFS is subject to four regions of reduced sensitivity. The first such region corresponds to large piston errors, as discussed following relation (15): As the piston error becomes large, the fringe modulation becomes dense and eventually exceeds the spectral resolution of DFS for all edge orientations. We discuss the other three regions of reduced sensitivity below. In the following paragraph we discuss the first of these regions, which corresponds to small piston errors and again applies to all edge orientations. The other two regions, which occur only when the intersegment edge is not parallel to the dispersion direction, are discussed in subsequent paragraphs.

Note that the right-hand side of Eq. (14) approaches a constant as γ approaches zero *or* as δ approaches zero. It follows that the fitting proce-

Fig. 3. Geometry of the primary mirror of the Keck telescopes, showing the 12 circular subapertures that sample the intersegment edges in the DFS mask. Each segment (A–D) is 0.90 m on a side. The subapertures are 12 cm in diameter. The 18 peripheral subapertures are used for pupil registration. The location of the grism with respect to the subapertures is indicated by the gray rectangle.

dure must break down for sufficiently small values of δ. (This problem is not apparent in Fig. 1 because the modulation is still mathematically well defined, even if it cannot practically be extracted by curve fitting in the presence of noise.) The problem manifests itself when the edge step produces approximately one fringe or less across the detector. To avoid this problem in the measurements described here, we conservatively exclude from consideration edge steps with $|\delta| \leq 1$ μm (corresponding to ~1.5 fringes or less). Alternatively, the problem could be dealt with by the deliberate introduction of an offset of ~1 μm for edges that produce small modulations.

All of the above analyses were conducted under the assumption that the intersegment edge was parallel to the dispersion direction. For hexagonal segments, this is of course not the case for all edges: There are edges at angles of not only 0° but also ±60° with respect to the dispersion direction. (As before, we always assume that the dispersion direction lies along the rows of the CCD.) Under these circumstances there are additional regions of reduced sensitivity, as described below.

The following discussion depends on the sign conventions used by DFS. We use the following conventions (see Fig. 3), which are determined by the orientation of the edge. Edge 7 (at an orientation of 0°) is positive if segment B lies above segment D, edge

5 (at an orientation of 60°) is positive if segment C lies above segment A, and edge 6 (at an orientation of −60°) is positive if segment B lies above segment C.

The case of an angle of ±60° between the edge (and hence the diffraction pattern) and the dispersion direction does not lend itself to the approximate treatment used above for 0° edges and is best pursued numerically. Figure 2 illustrates the formation of a fringe for three different edge angles. For each edge angle, a pair of numerically simulated fringes is shown. In the lower one of each pair, the fringe is sparsely sampled at a number of discrete wavelengths in order to provide some insight into how the fringe is built up from a continuous spectrum of wavelengths. In the upper fringe of each pair, the wavelength sampling is dense, and the individual diffraction patterns are blurred together to form a dispersed fringe. Note that the orientation of the diffraction pattern for a positive edge step at an edge angle of 60° (top trace in Fig. 2) is such that it tends to fill in the dark bands in the fringe and significantly reduce the fringe visibility. Thus edges at 60° are relatively insensitive to positive edge steps, and edges at −60° are similarly insensitive to negative edge steps. Fringe visibilities for all three orientations as determined from the simulations are presented in Fig. 1. This ±60° effect (which is confirmed in the experiments described below) represents a complication for DFS in the current implementation. It can be addressed, for example, by splitting the beam, by using different grisms for different orientations, or by using a more complicated mask geometry, but we do not pursue such remedies here.

3. Hardware Description

A. Keck Telescopes

Except for their instrumentation, the two Keck telescopes[7] are virtually identical. The experiments described in this work were carried out at the Keck 2 telescope. The primary mirror of each Keck telescope consists of 36 hexagonal segments, each 90 cm on a side, and an active control system (ACS) of sensors and actuators that freezes the relative positions of the segments, thereby stabilizing the structure against gravity and thermal effects. The ACS can also be used to introduce specific misalignments into the primary mirror in a controlled way, as was done in the experiments described here. Note that there is no absolute optical reference in the ACS; the ACS stabilizes the sensor readings at their desired values once they are determined, but these desired values must be determined by independent optical means. The PCS, described below, was developed for this purpose.

B. Phasing Camera System

The Keck PCS[6] is a Shack–Hartmann-type wavefront sensor, which is permanently mounted at one of the bent Cassegrain focal stations of each of the Keck telescopes. The PCS optics reimages the primary

mirror at a magnification of 1/200 in the collimated beam. A mask at the position of the reimaged primary mirror defines the circular subapertures of diameter $d = 12$ cm (referred to the primary mirror) at the center of each of the intersegment edges. Immediately following the mask, in normal operations, is an array of 2 mm $\times$ 3 mm prisms. The mask and prisms form an integral subassembly, which can be reproducibly inserted into the collimated beam with a wheel and detent mechanism. The prisms, in combination with a single objective lens, map the collimated subbeams onto a 1024×1024 pixel CCD in a pattern that replicates the geometry of the primary mirror. The size of the subapertures is chosen to be significantly smaller than the atmospheric coherence diameter r_0, of ~ 20 cm at a wavelength of 0.5 μm, so that atmospheric turbulence represents only a small perturbation to the overall wave front.

The mask–pupil registration is critical to this modified Shack–Hartmann scheme, because the subapertures must be accurately aligned with respect to the intersegment edges. We measure this registration (and monitor it with every CCD exposure) by means of additional subapertures on the outer segment edges. Details of the registration procedure are given elsewhere.[1] Typical registration accuracy of the mask is $\pm 0.03°$ of rotation and ± 1.2 mm of translation in each dimension (referred to the primary mirror).

With a single exposure on a moderately bright star (typically fourth to seventh magnitude), we obtain a well-separated subimage or diffraction pattern on the detector for each unobscured intersegment edge. The diffraction patterns are of the order λ/d or 1 arc sec in width. The image scale on the detector is 6.50 pixels/arc sec.

C. Dispersed Fringe Sensing Implementation into the Phasing Camera System

For the DFS measurements performed here, we fabricated an alternative subassembly with a mask followed by a single lens and a grism, with the single lens replacing the usual prism array. The new subassembly was inserted into a spare position in the wheel and detent mechanism described above. The dispersion direction of the grism was aligned with the rows of the CCD. To optimize the maximum detectable piston error over the PCS field-of-view and wavelength operating range, we selected a grism with 150 grooves/mm and a central wavelength of 650 nm.

The DFS mask was similar to the normal PCS mask, except that only 12 of the subapertures (generally 1 in each row) were left clear so that the dispersed fringes from the other subapertures in the row would not run into one another (Fig. 3). To investigate the effects of fringe crowding, we spaced several of the subapertures conservatively far apart from one another in the vertical direction (1–6 and 12 in Fig. 3), whereas others were spaced closer together (7–11). Selected subapertures include segment edges at 0°, +60°, and −60° to enable us to investigate the dependence of the fringe visibility on the sign of the
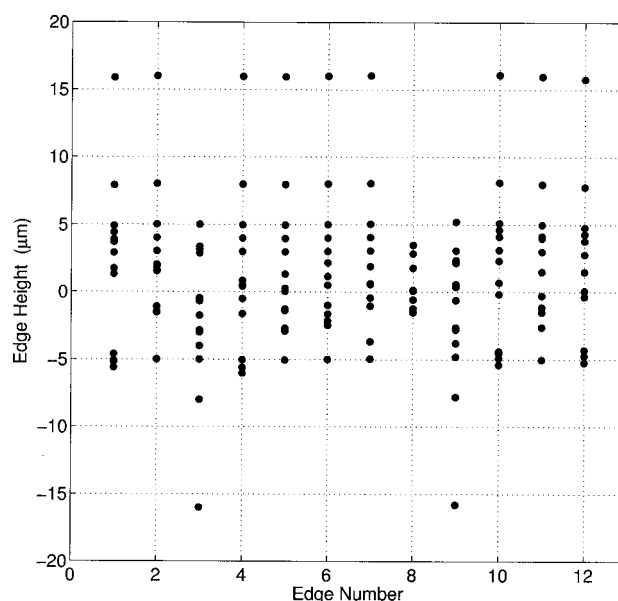

Fig. 4. Edge-height distribution for all experimental trials.

edge step. Light from 18 of the peripheral subapertures did not pass through the grism but did pass through the mask, enabling these peripheral spots to be used for mask–pupil registration.

4. Experimental Procedure

The Keck telescopes are normally phased by use of the broadband phasing procedure,[1] which has a capture range of 30 μm and an accuracy of 30 nm. For the most accurate work, the phasing is refined by use of the narrowband algorithm,[2] which has an accuracy of 10 nm but a capture range of only ~ 200 nm. For the experiments conducted here, the telescope segments were aligned in tip–tilt and then accurately phased with the broadband algorithm followed by the narrowband algorithm. We then used the telescope ACS to produce a variety of primary mirror configurations consisting of pure segment piston errors. Both random and nonrandom primary mirror configurations were used. Figure 4 shows the distribution of all the edge heights (0.5–16 μm) that were studied in this experiment. In the nonrandom configurations, all nonzero edge heights had the same value. For the particular DFS mask used in this work, subaperture 8 had an edge height of zero in the nonrandom configurations; these cases were excluded from the analysis in Section 6.

Because there was some uncertainty about the absolute accuracy of the ACS, the edge heights in these misphased configurations were measured directly by use of the PCS single-wavelength narrowband algorithm ($\lambda = 852$ nm). In most cases these edge heights exceeded the formal capture range of this algorithm, but the correct phase was "unwrapped" by use of the fact that the edge height was approximately known from the ACS dephasing command. (The same results could have been achieved by preceding the narrowband algorithm with the broad-
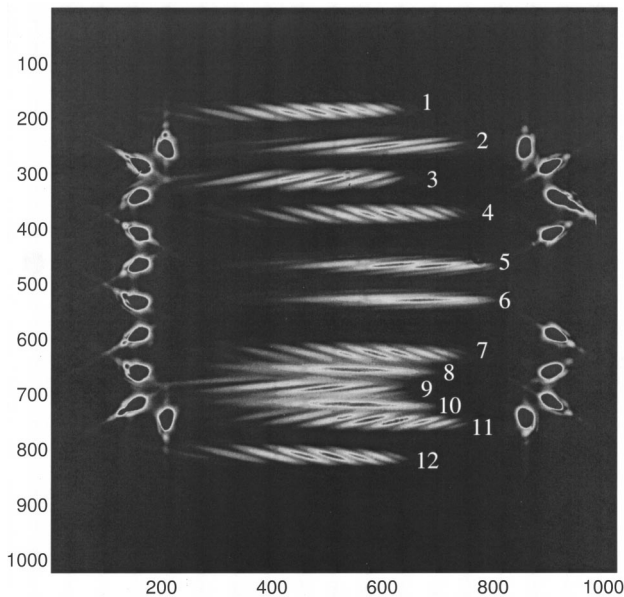
Fig. 5. Sample DFS image showing 12 dispersed fringes from the intersegment edges as well as 18 peripheral spots (undispersed) used for pupil registration. The display has been stretched in order to accentuate the fringes.
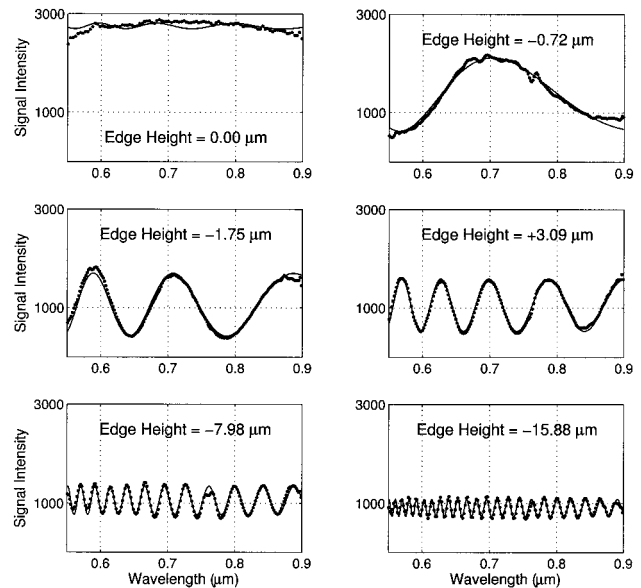

Fig. 6. Sample DFS signal intensities for edge 3 (at an orientation of 0°), depicting a range of piston values. The corresponding fits to Eq. (14) are also shown. The upper-left plot is an example of two segments that are nearly phased; such results are discarded by the fitting algorithm because the calculated fringe contrast is too low. Also, as the absolute piston value increases, the fringe visibility decreases as a result of the limited spectral resolution, thereby defining the DFS capture range.

5. Data Processing and Analysis

As shown in Fig. 5, each DFS image contains dispersed fringes from the 12 intersegment subapertures as well as the 18 undispersed peripheral spots for pupil registration. The mean background level, computed from the dark regions near the upper and lower parts of each image, was subtracted out as the dark background. The centroid positions of the peripheral spots were used to shift and recenter each image.

The wavelength scale on the detector was calibrated with three narrowband filters centered at 619, 651, and 891 nm (full width at half-maximum of 10 nm). To be conservative, we computed the wavelength calibration separately for each of the 12 subapertures. A maximum 2.4% variation in the dispersion was observed, depending on the subaperture position from the center.

The DFS signals contain spectral information from both the star and the instrument, as well as modulation from the piston error. We removed unwanted spectral features of the star and the instrument by dividing out a reference fringe that contained no piston modulation. The reference fringe image was acquired by translation of the pupil in x and y (by use of a pupil steering mechanism inside the PCS) such that the subapertures on the mask coincided with the segment centers (where the piston error is zero) rather than with the intersegment edges. After the reference spectrum was removed from the raw DFS signal, the processed signal contained only the modulation from the piston error. As described in Section 2, the

intensity signals were then fit to the fringe equation by means of a least-squares method.

6. Results

Figure 6 shows the processed signals and the corresponding best-fit theoretical curves for a typical edge. For this edge (number 3) the orientation is 0°, so the fringes are visible for both positive and negative edge steps. As predicted, the visibility decreases with increasing edge step. The experimental visibilities are lower than the theoretical curve in Fig. 1, probably because of aberrations in the optical system as well as atmospheric seeing.

The fitting algorithm monitors the best-fit amplitude and visibility in order to determine the quality of the piston solution. If the fitted amplitude is unreasonably large or the visibility too small, the algorithm will ignore the measurement (see the upper-left plot in Fig. 6). This prevents the algorithm from mistakenly fitting to the noise in the fringe in cases where the fringe visibility is very low compared with the noise level, such as when the segments are nearly phased or in the presence of large segment aberrations.[4,5]

Figure 7 compares the DFS detected edge heights with the corresponding PCS measurements. The results agree to within 2% for piston errors ranging from 1 to 16 μm. Edge-height measurements for edges that were nearly phased ($|\delta| \leq 1\,\mu m$) or had low fringe visibilities as a result of the ±60° effect (see Section 2) were eliminated from consideration.

Although we did not include them in the above

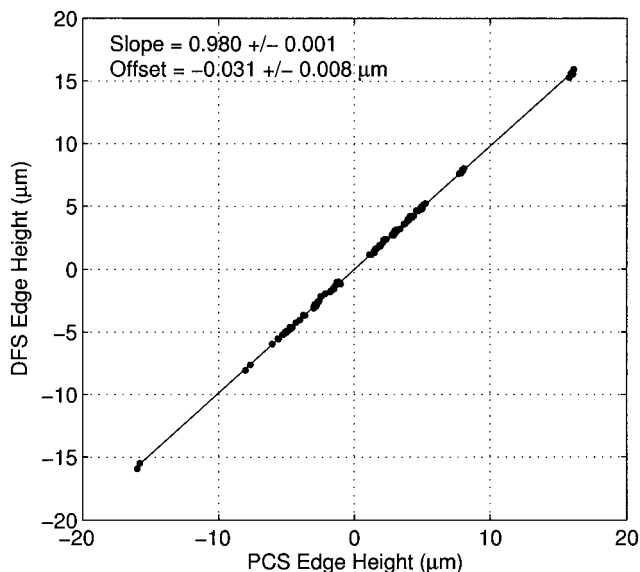band algorithm, but this would have been more time consuming.)

Fig. 7. DFS measurements compared with PCS measurements, excluding the data points corresponding to the three regions of reduced sensitivity, as described in the text. The best straight-line fit yields a slope that is close to unity (0.980 ± 0.001) and a systematic offset of −0.031 ± 0.008 μm.

analysis, we did analyze those edges oriented at ±60° that fell into the two regions of reduced sensitivity specific to their orientation. Figure 8 depicts six DFS signals with similar absolute edge heights, but with different signs and edge orientations. As expected, when the edge was oriented at 60°, the fringe was washed out if the edge height was +5 μm. Similar results were obtained for edges at −60° with a
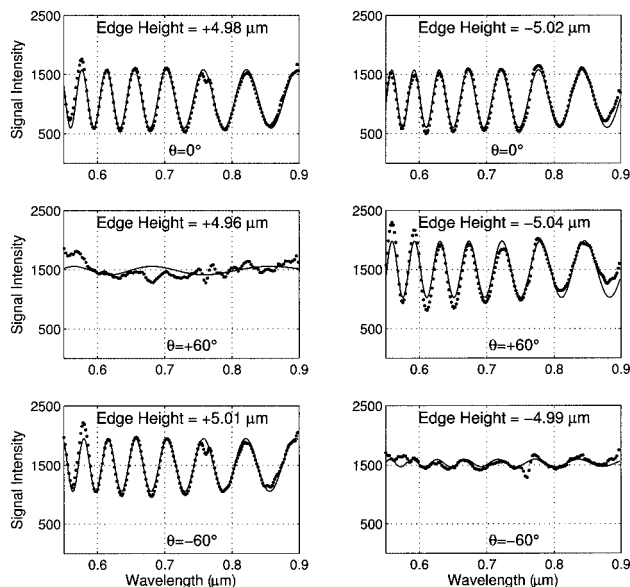
Fig. 8. Comparison of the fringe visibility for positive edge heights (left column) and negative edge heights (right column) for various edge orientations. For edge orientations of ±60° (but not for 0°), the fringe visibility is sensitive to the sign of the edge height, as shown in the middle row (60° edge orientation) and bottom row (−60° edge orientation).

Table 1. Summary of DFS Intersegment Height Measurements[a]

Edge Number	Number of Measurements	Final rms Piston Error	
		Uncorrected (μm)	Corrected (μm)
1	16	0.141	0.047
2	16	0.116	0.069
3	14	0.128	0.115
4	11	0.154	0.041
5	6	0.141	0.129
6	12	0.158	0.153
7	12	0.183	0.079
8	2	0.113	0.119
9	13	0.100	0.073
10	7	0.079	0.142
11	15	0.158	0.053
12	14	0.164	0.071

[a]Errors are given with respect to PCS: The uncorrected final rms piston error is calculated without the systemic trend removed; the corrected final rms piston error is calculated with the global systematic trend removed. For the initial height distribution, see Fig. 4.

height of −5 μm. Further considerations on the sensitivity of the fringe visibility to the sign of the piston error for nonparallel edge orientations have been presented elsewhere.[5]

The DFS detection errors (DFS minus PCS measurements) are summarized in Table 1. An examination of the DFS versus PCS differences reveals a systematic trend in the residual error that is linearly proportional to the initial segment piston. The systematic error was observed in all 12 edges, with a mean value of 20 nm/μm or 2.0% (Fig. 9). After the best-fit straight line was removed, the detection error was significantly reduced (see the last column in Table 1). We have considered that the DFS–PCS discrepancy might originate on the PCS side, but this
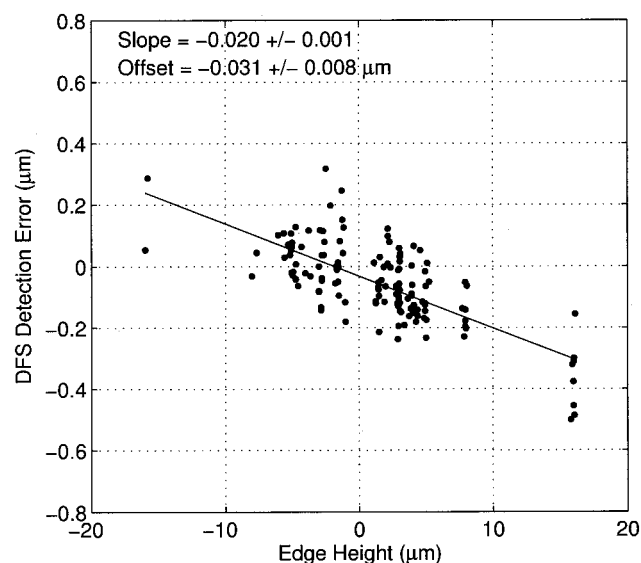

Fig. 9. DFS detection error (relative to PCS) versus edge height, excluding the data points corresponding to the three regions of reduced sensitivity. The best straight-line fit is also plotted.

does not seem to be the case. To demonstrate this, we compared the PCS measurements to those inferred from the ACS commands. Although the Keck ACS has never been calibrated against PCS (so that the ACS commands and PCS measurements are in fact independent), the systematic difference between PCS and ACS was found to be 0.2% ± 0.1%. In view of this agreement, it is reasonable to attribute virtually the entire DFS–PCS systematic difference to DFS. This systematic discrepancy between DFS and PCS is likely due to a systematic error in the DFS wavelength calibration. This error may result from chromatic aberration in the PCS optics (which are designed to minimize chromatic effects only upstream from the exit pupil), from an offset between the average position on the detector of the star and the calibration source, or from an interaction between these effects.

As described in Section 3, the subapertures in the DFS mask were selected to investigate the effect of fringe crowding on the piston detection error. Our results indicate that there is no noticeable difference in the detection between fringes that are well separated and those that are closely spaced. This is because the fringes are well sampled (approximately 7 pixels across λ/d), whereas (except for the sign extraction) the DFS signal requires only a single row of pixels extracted from the center of the fringe.

7. Conclusions

In this experiment we used DFS to accurately measure segment piston errors ranging from approximately one wave ($\sim$1 μm) to as much as 16 μm. Only a single broadband measurement was necessary to measure multiple edges in parallel. Benchmarked against PCS, DFS is highly accurate for measuring segment pistons, with an rms error (averaged over all 12 subapertures) of $\sim$142 nm. With improved calibration procedures, the accuracy would be 90 nm or less.

In summary, the high level of agreement between the DFS and the PCS results presented here provides strong validation of the DFS algorithm under realistic conditions for a large segmented mirror telescope.

These observations highlight both the high level of efficiency of DFS and the need for accurate wavelength calibration.

References

1. G. A. Chanan, M. Troy, F. G. Dekens, S. Michaels, J. Nelson, T. Mast, and D. Kirkman, "Phasing the mirror segments of the Keck telescopes: the broadband phasing algorithm," Appl. Opt. **37,** 140–155 (1998).
2. G. A. Chanan, C. Ohara, and M. Troy, "Phasing the mirror segments of the Keck telescopes II: the narrow-band phasing algorithm," Appl. Opt. **39,** 4706–4714 (2000).
3. G. Chanan, M. Troy, and E. Sirko, "Phase discontinuity sensing: a method for phasing segmented mirrors in the infrared," Appl. Opt. **38,** 704–713 (1999).
4. F. Shi, D. C. Redding, C. W. Bowers, A. E. Lowman, S. A. Basinger, T. A. Norton, P. Petrone III, P. S. Davila, M. E. Wilson, and R. A. Boucarut, "DCATT dispersed fringe sensor: modeling and experimenting with the transmissive phase plates," in *UV, Optical, and IR Space Telescopes and Instruments*, J. B. Breckinridge and P. Jakobsen, eds., Proc. SPIE **4013,** 757–762 (2000).
5. F. Shi, D. C. Redding, A. E. Lowman, C. W. Bowers, L. A. Burns, P. Petrone III, C. M. Ohara, and S. A. Basinger, "Segmented mirror coarse phasing with a dispersed fringe sensor: experiments on NGST's Wavefront Control Testbed," in *IR Space Telescopes and Instruments*, J. C. Mather, ed., Proc. SPIE **4850,** 318–328 (2002).
6. G. A. Chanan, "Design of the Keck Observatory alignment camera," in *Precision Instrument Design*, T. C. Bristow and A. E. Hatheway, eds., Proc. SPIE **1036,** 59–70 (1988).
7. J. E. Nelson, T. S. Mast, and S. M. Faber, "The design of the Keck Observatory and Telescope," Keck Observatory Report 90 (W. M. Keck Observatory, Kamuela, Hawaii, 1985).